


The effect of charge transfer transition on the photostability of lanthanide-doped indium oxide thin-film transistors

Penghui He¹, Hua Xu¹, Linfeng Lan¹, Caihao Deng¹, Yongbo Wu¹, Yilong Lin¹, Siting Chen¹, Chunchun Ding¹, Xiao Li¹, Miao Xu¹ & Junbiao Peng¹

Amorphous oxide semiconductors are promising for their use in thin-film transistor (TFT) devices due to their high carrier mobility and large-area uniformity. However, their commercialization is limited by the negative gate bias stress experienced under continuous light illumination. Here, we report an approach to improve the negative bias illumination stress (NBIS) stability of amorphous oxide semiconductors TFTs by using lanthanide-doped indium oxide semiconductors as the channel layer. The effect of different lanthanide dopants on performances of solution-processed Ln:In₂O₃ TFTs are investigated. All lanthanides exhibit strong suppression of oxygen vacancy, which shift the V_{on} from -13.5 V of pure In₂O₃ TFT to -1 – 1 V of Ln:In₂O₃ TFTs (except Ce). However, only Pr:In₂O₃ and Tb:In₂O₃ TFTs exhibit much better NBIS stability with same ΔV_{on} of -3.0 V, compared to much higher ΔV_{on} of -7.9 – -15.6 V for other Ln:In₂O₃ TFTs. Our comprehensive study reveals that praseodymium and terbium act as a blue light down-conversion medium with low charge transfer transition energy for lowering photosensitivity of oxide semiconductors.

¹State Key Laboratory of Luminescent Materials and Devices, South China University of Technology, Guangzhou, China. ✉email: lanlinfeng@scut.edu.cn

Amorphous oxide semiconductors (AOSs) have attracted considerable attention, owing to their outstanding properties, such as high carrier mobility with large-area uniformity, low off-state current (I_{off}), and large optical bandgap^{1,2}. However, there is a serious issue limiting further commercialization applications of AOS TFTs that serious threshold voltage shift (ΔV_{th}) is observed when the TFTs experience a negative gate bias stress combined with continuous light illumination even in the visible spectrum (NBIS), which cannot be fully recovered even after removing the stress for days^{3–5}.

It is widely accepted that the NBIS instability is attributed to the intrinsic states of AOS materials regardless of the device structures. Several degradation models are proposed to reveal the mechanism of the NBIS instability of the AOS TFTs, including the trapping of photogenerated holes^{6–9}, the creation of ionized oxygen vacancy (Vo) defects^{10,11}, the formation of metastable peroxides¹², the self-trapping of holes by polarons¹³, etc.

To improve the NBIS stability of AOS TFTs, reducing concentration of preexisting Vo defects (subgap states) is the most commonly used method. The cation (oxygen binder) doping^{14–16}, and the intentional supply of oxygen species, such as high-pressure annealing (HPA)^{17–19}, oxygen-containing plasma treatment²⁰, ozone radical treatment²¹, and ultra-high vacuum sputtering²², would result in a decrease in Vo. However, the improved V_{th} shift is still too large to drive active-matrix displays without compensation^{5,22,23}. J. Kim and H. Hosono et al.²² developed a wide-bandgap AOS (ZnGaO) to improve the NBIS stability of the AOS TFTs by widening the optical bandgap to keep the photoexcitation energy between the subgap states and the conduction band minimum (CBM) larger than ~ 3 eV. However, this approach will decrease the mobility seriously, because the 4s orbitals of adjacent metal ions (both Ga and Zn) do not overlap that would destroy the electron transport paths in the amorphous state. Therefore, there is a tradeoff between the mobility and NBIS stability of the AOS TFTs.

Here, we report an approach to improve the NBIS stability of AOS TFTs by using lanthanide-doped indium oxide ($\text{Ln}:\text{In}_2\text{O}_3$) semiconductors as the channel layer. It is found that only praseodymium (Pr) and terbium (Tb) can improve the NBIS stability of the AOS TFTs greatly, and doping Pr/Tb into In_2O_3 would not affect the mobility much, so the tradeoff between the mobility and NBIS stability of the AOS TFTs can be broken. Comprehensive studies reveal that different lanthanides (Lns) have a different effect on the NBIS stability of AOS TFTs, and Pr/Tb acts not only a Vo suppressant but also a blue light downconversion medium with low charge transfer transition energy. The result is different from those reported elsewhere, where the lanthanides are merely regarded as free carrier suppressants of the AOSs due to ultra-low electronegativities^{24–30}. T. Kamiya et al.^{31,32} gave a comprehensive study on the effect of the Ln doping on the photoluminescence characteristics of the AOS films but the effect of Ln doping on the TFT characteristics has not been investigated. It is should be noted that promethium (Pm) is not included in this work because of its radioactivity.

Results and discussion

The absorption characteristics of the different Ln ions. As known, lanthanides have electron configurations of $[\text{Xe}] 4f^n 5d^m 6s^2$ ($n = 0–14$, $m = 0–10$). The unfilled 4f orbitals form complicated energy level structures due to Coulomb interactions, spin-orbit coupling, and external field interactions. Lanthanides exhibit various optical properties which are attributed to $f-f$ transition, $f-d$ transition, or charge transfer transition (electrons transit between the ligands and Ln ions). Figure 1 shows the photos of the different aqueous $\text{Ln}(\text{NO}_3)_3 \cdot n\text{H}_2\text{O}$ solutions (0.4 M)

and the corresponding spin-coated thin films annealed at 300 °C. Only $\text{Pr}(\text{NO}_3)_3 \cdot n\text{H}_2\text{O}$, $\text{Nd}(\text{NO}_3)_3 \cdot n\text{H}_2\text{O}$, $\text{Ho}(\text{NO}_3)_3 \cdot n\text{H}_2\text{O}$, and $\text{Er}(\text{NO}_3)_3 \cdot n\text{H}_2\text{O}$ solutions show light colors, which are attributed to the $f-f$ transition of the Pr, Nd, Ho, and Er ions. Figure 2a shows the absorption spectra of the different aqueous $\text{Ln}(\text{NO}_3)_3 \cdot n\text{H}_2\text{O}$ solutions. Typical $f-f$ sharp absorption peaks are seen in $\text{Pr}(\text{NO}_3)_3 \cdot n\text{H}_2\text{O}$, $\text{Nd}(\text{NO}_3)_3 \cdot n\text{H}_2\text{O}$, $\text{Ho}(\text{NO}_3)_3 \cdot n\text{H}_2\text{O}$, and $\text{Er}(\text{NO}_3)_3 \cdot n\text{H}_2\text{O}$ solution (much weaker absorptions peaks are also seen in $\text{Sm}(\text{NO}_3)_3 \cdot n\text{H}_2\text{O}$, $\text{Eu}(\text{NO}_3)_3 \cdot n\text{H}_2\text{O}$, $\text{Dy}(\text{NO}_3)_3 \cdot n\text{H}_2\text{O}$, and $\text{Tm}(\text{NO}_3)_3 \cdot n\text{H}_2\text{O}$ solutions), which are in consistent with the colors of the solutions.

Interestingly, after the precursors are spin-coated onto the glass substrates and annealed at 300 °C, all the films are colorless and transparent except PrO_x and TbO_x . To investigate the color difference between the solution and the corresponding film, UV-visible light absorption was measured for all of the LnO_x films, as shown in Fig. 2b. The CeO_x , PrO_x , and TbO_x films exhibit broad-band absorption, while the other films are transparent to the light with the wavelength longer than 300 nm. For the CeO_x film, the absorption is strong with a peak centered at ~ 300 nm and a cut-off edge at ~ 390 nm. For the PrO_x and TbO_x films, the absorption peaks are broadened into the visible light without distinct cut-off edges. The broad-band and strong absorption implies that the absorption cannot be caused by $f-f$ transition, because $f-f$ transition has some features, including i) $f-f$ transition is forbidden due to the same parity, so the $f-f$ transition absorption is relatively weak; ii) $f-f$ transition spectrum is line spectrum with sharp peaks because the intimal 4f orbitals are screened by the outer 5d and 6s orbitals and hardly influenced by the chemical environment; iii) $f-f$ transition can be observed in most of the Ln ions. The absorption spectra of CeO_x , PrO_x , and TbO_x films is similar to that reported by D.E. Hobart et al.³³ in 1980 (see Fig. 2c–e), who ascribed the broad-band and absorption to the charge transfer transition between the delocalized ligand molecular orbital and the Ln^{4+} ion. Therefore, it is reasonable to deduce that Ce^{4+} , Pr^{4+} , and Tb^{4+} ions exist in the solid films but cannot exist in the aqueous $\text{Ln}(\text{NO}_3)_3 \cdot n\text{H}_2\text{O}$ solutions. The oxidation from Ln^{3+} to Ln^{4+} is considered to be taken place during the 300 °C annealing step because all of the as-spin-coated LnO_x films without annealing are colorless and transparent. As known, nitrate (NO_3^-) can releases oxygen-free radicals at a relatively low temperature (~ 200 °C)³⁴. The oxygen radicals with strong oxidability can help oxidizing the Ce^{3+} , Pr^{3+} , and Tb^{3+} ions to the tetravalent oxidation state. Compared to the work by D.E. Hobart et al.³³, the absorption spectra for the PrO_x and TbO_x films in this work span a much wider range (extend to the near-infrared region), which may be attributed to the larger metal-ligand electron cloud overlap in the solid state. Moreover, the oxygen vacancies and structural defects of the amorphous LnO_x films will give rise to the electron cloud expansion effect and further broaden the absorption spectra to the near-infrared region, as discussed later.

To further analyze, the valence state of the CeO_x , PrO_x , and TbO_x films, X-ray photoelectron spectroscopy (XPS) experiments were carried out, as shown in Supplementary Fig. 1. It can be found that the Ce ions in the CeO_x film are mainly in the tetravalent state (Ce^{4+}) with only a small part of trivalent Ce ions (Ce^{3+} , see $V^{\prime}-W^{\prime}$ peaks in Supplementary Fig. 1), while the number of $\text{Pr}^{3+}/\text{Tb}^{3+}$ ions is comparable to that of $\text{Pr}^{4+}/\text{Tb}^{4+}$ ions in the $\text{PrO}_x/\text{TbO}_x$ films (Supplementary Fig. 1).

The performances of the pure In_2O_3 TFTs. To investigate the effect of different lanthanide doping on the performance of the AOS TFTs, different lanthanide elements are doped into In_2O_3 by mixing $\text{Ln}(\text{NO}_3)_3 \cdot n\text{H}_2\text{O}$ and $\text{In}(\text{NO}_3)_3 \cdot n\text{H}_2\text{O}$ solutions together to

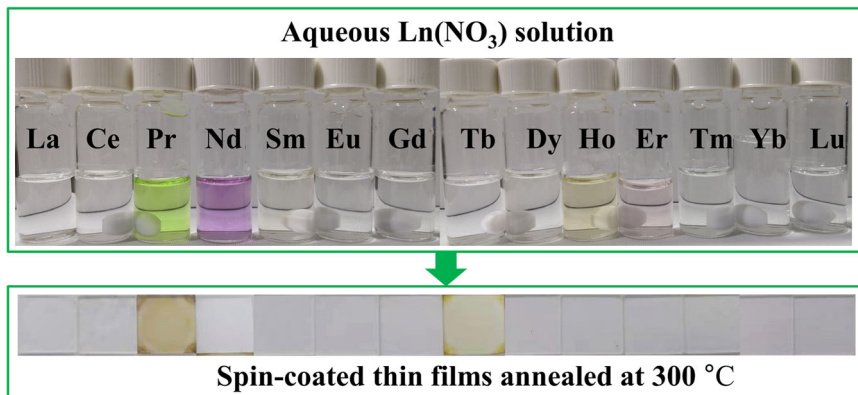


Fig. 1 $\text{Ln}(\text{NO}_3)_3 \cdot n\text{H}_2\text{O}$ aqueous solutions and LnO_x films. The photos of the different aqueous $\text{Ln}(\text{NO}_3)_3 \cdot n\text{H}_2\text{O}$ solutions (0.4 M) and the corresponding spin-coated films annealed at 300 °C.

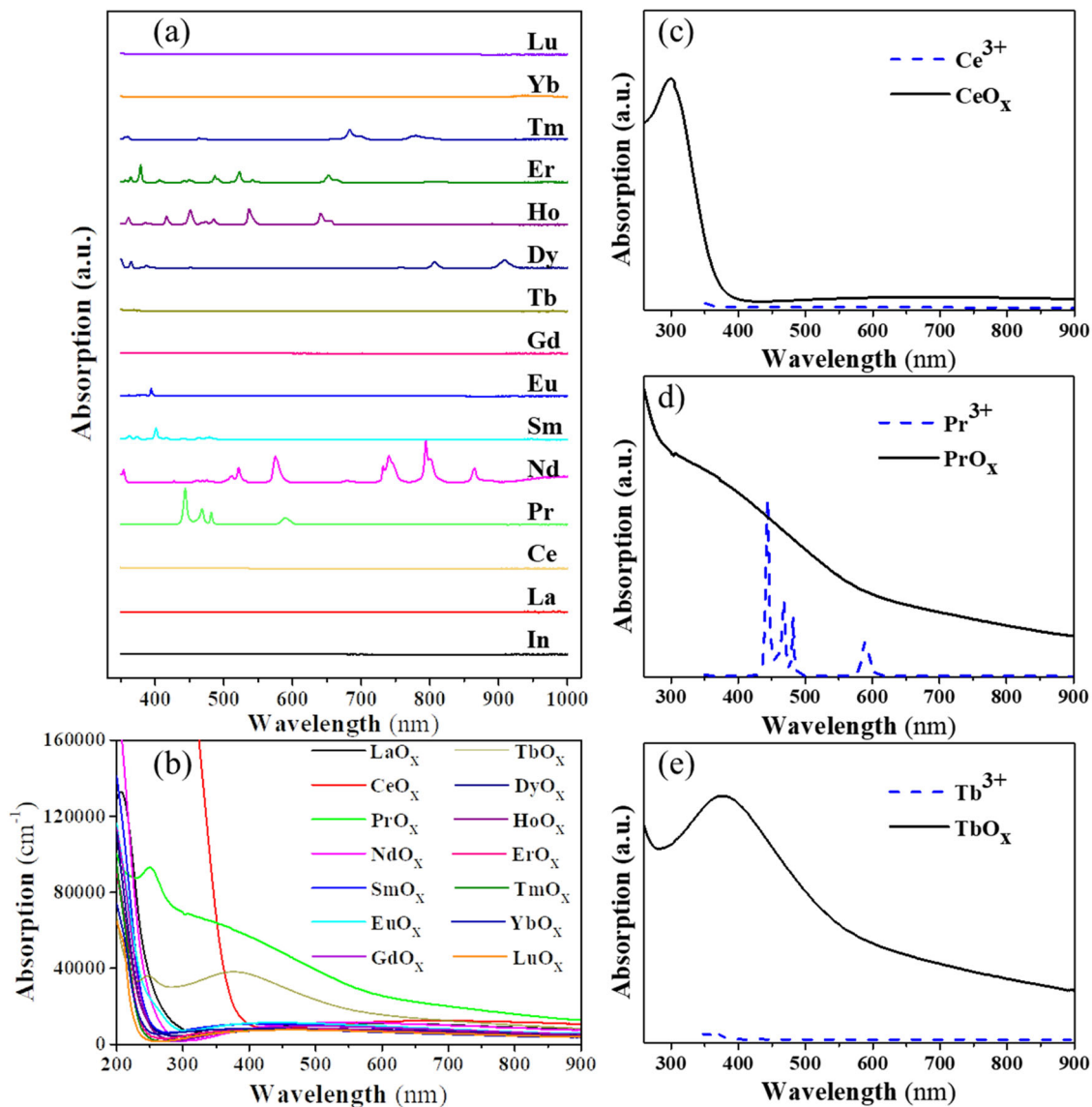


Fig. 2 The absorption of $\text{Ln}(\text{NO}_3)_3 \cdot n\text{H}_2\text{O}$ aqueous solutions and LnO_x films. **a** the absorption spectra of the different $\text{Ln}(\text{NO}_3)_3 \cdot n\text{H}_2\text{O}$ and $\text{In}(\text{NO}_3)_3 \cdot n\text{H}_2\text{O}$ aqueous solutions. **b** UV-visible light absorption of the different LnO_x films based on spin-coating $\text{Ln}(\text{NO}_3)_3 \cdot n\text{H}_2\text{O}$ aqueous solutions annealed at 300 °C. **c-d** UV-visible light absorption of **c** Ce^{3+} and CeO_x , **d** Pr^{3+} and PrO_x , and **e** Tb^{3+} and TbO_x .

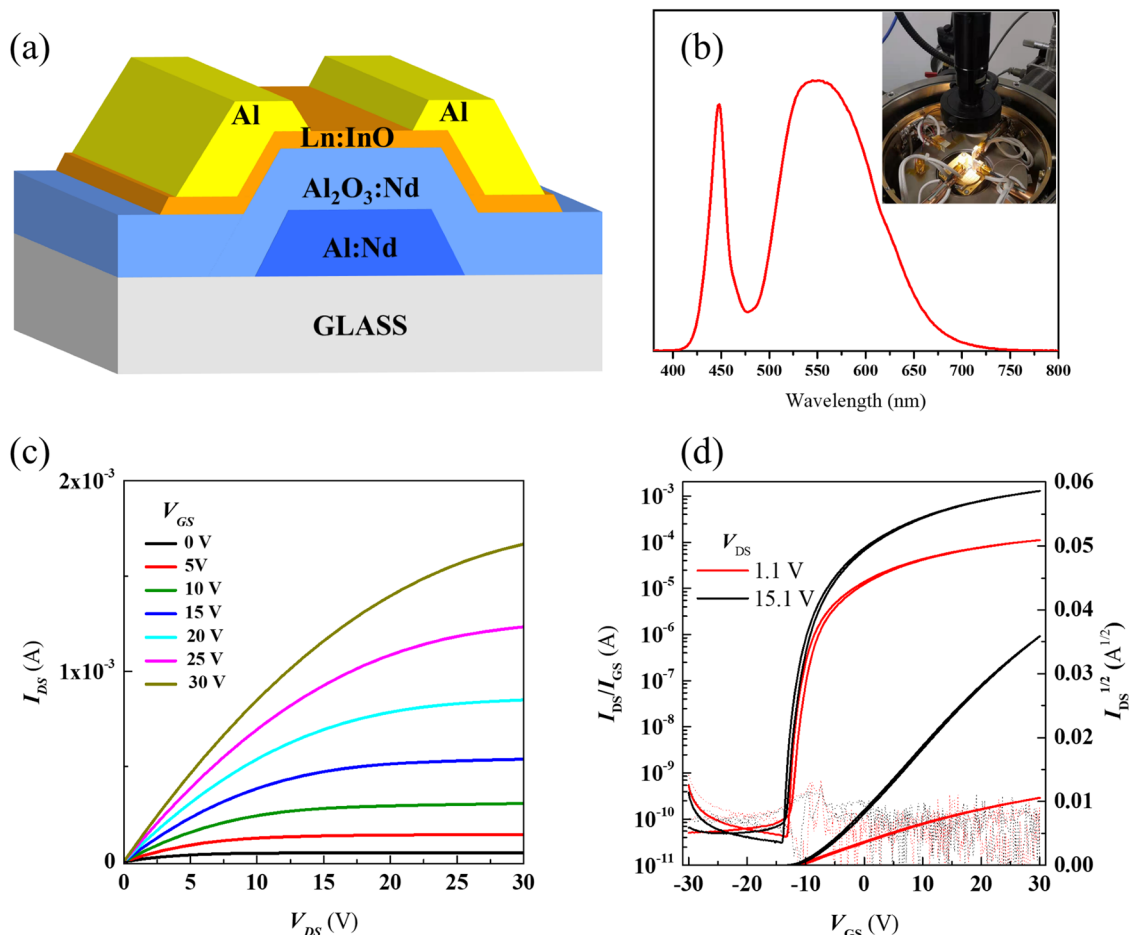


Fig. 3 The characteristics of pure In_2O_3 TFT. **a** Device structure of TFTs based on solution-processed In_2O_3 or Ln: In_2O_3 semiconductors without any passivation. **b** LED spectrum for the NBIS test. **c** output and **d** transfer characteristics of the undoped In_2O_3 TFT annealed at 300°C with an aqueous precursor solution. The transfer characteristics of TFTs were measured at $V_{\text{DS}} = 1.1$ and 15.1 V, respectively, and V_{GS} swept from -30 to 30 V, while output characteristics were tested when V_{GS} was held at different voltages between 0 and 30 V in step of 5 V, and V_{DS} swept from 0 to 30 V at each V_{GS} .

form precursor solutions. The In/Ln molar ratio was optimized to be 19:1 (5 at.% of Ln). Bottom-gate and top-contact TFTs with undoped In_2O_3 or Ln: In_2O_3 channel layers were fabricated by spin-coating In_2O_3 or Ln: In_2O_3 aqueous precursor solutions and annealing at $300/350^\circ\text{C}$ in air condition for 1 h (see Fig. 3a). To avoid the influence of the air molecules on the stability of the AOS TFTs, all the TFTs were tested under vacuum condition. Figure 3c, d show output and transfer characteristics of the undoped In_2O_3 TFT. The mobility is extracted from transfer characteristics at $V_{\text{DS}} = 15.1$ V to be $17.1 \text{ cm}^2 \text{ V}^{-1} \text{ s}^{-1}$, which indicates that the indium nitrate aqueous precursor can form a continuous mate oxide skeleton by thermal decomposition even at a low temperature of 300°C . However, the undoped In_2O_3 TFT exhibits highly conductive with a turn-on voltage (V_{on} , defined as the V_{GS} when I_{DS} is increase to 1 nA) of as negative as -13.3 V, which is due to the large amounts of free carriers resulted from the high-density oxygen vacancies in the undoped In_2O_3 film³⁵. In addition, the undoped In_2O_3 TFT shows serious stability problems as discussed later.

The transfer characteristic of the AOS TFTs based on Ln: In_2O_3 . Figure 4 shows the transfer characteristic curves of the TFTs based on 14 Ln: In_2O_3 annealed at 300°C . All the TFTs exhibit excellent gate-controlled field-effect characteristics except Ce: In_2O_3 TFT (see Supplementary Fig. 2) that will be discussed later. Compared to the undoped In_2O_3 TFT, which has a

Table 1 Summary for the performance of TFTs with Ln: In_2O_3 channels.

Dopant	μ @ 350°C ($\text{cm}^2 \text{ V}^{-1} \text{ s}^{-1}$)	V_{on} (V)	μ @ 300°C ($\text{cm}^2 \text{ V}^{-1} \text{ s}^{-1}$)	V_{on} (V)	NBIS ΔV_{on} (V)
La	8.3	-4.1	3.5	-1.0	-7.9
Ce	-	-	-	-	-
Pr	12.2	-3.7	4.3	-0.5	-3.0
Nd	8.2	-1.7	3.1	1.0	-8.0
Sm	13.7	-5.6	4.2	0.1	-12.4
Eu	7.6	-3.2	4.3	-0.4	-12.8
Gd	16.2	-6.9	4.7	-0.2	-13.9
Tb	12.7	-3.2	5.2	-0.8	-3.0
Dy	15.3	-3.4	4.3	-0.2	-15.6
Ho	14.8	-3.7	4.0	-0.4	-11.9
Er	13.2	-3.6	4.7	-1.0	-9.0
Tm	10.1	-3.5	6.1	-0.1	-14.7
Yb	6.0	-3.9	4.8	-0.8	-14.9
Lu	14.3	-3.5	4.1	-0.5	-11.9

V_{on} of -13.3 V, the Ln: In_2O_3 TFTs have more positive V_{on} that range from -1 to 1 V (see Table 1) and steeper SS, revealing that Ln doping with a concentration of only 5 at.% can suppress Vo generation and decrease free carrier concentration substantially.

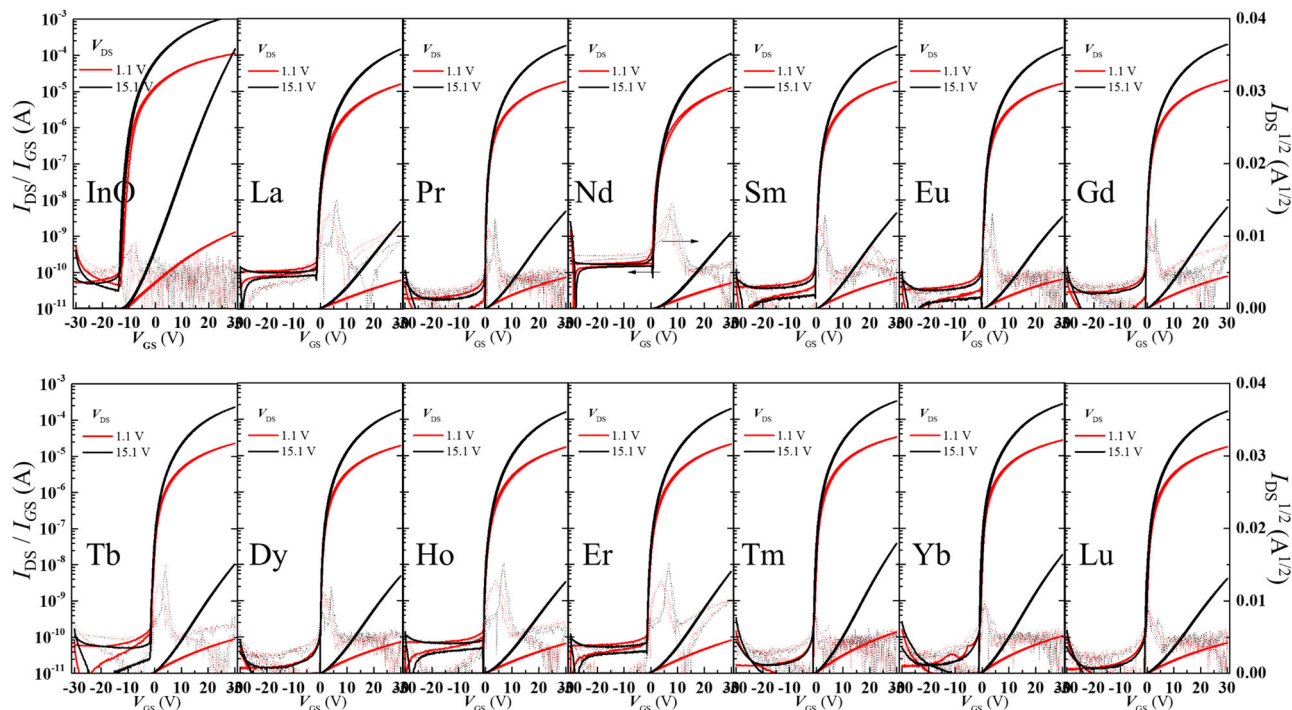


Fig. 4 Transfer characteristics of Ln:In₂O₃ TFTs. Transfer characteristics of TFTs based on spin-coating Ln:In₂O₃ aqueous precursor solutions with annealing at 300 °C in air condition, the V_{DS} was held at 1.1 V (red curve) and 15.1 V (black curve), respectively, and the V_{GS} sweep from -30 to 30 V.

In conventional AOS (IGZO), the concentration of the free carrier suppressant (Ga) should be very high (33.3 at.%), because Ga is not a strong free carrier suppressant. The electronegativity of Ga is 1.6 with Ga–O dissociation energy of 374 kJ mol⁻¹, no much difference compared to In (the electronegativity of In is 1.7 with In–O dissociation energy of 346 kJ mol⁻¹). High Ga concentration will destroy overlaying of the In 5s orbitals (especially in the amorphous state), and result in electron mobility decrease. Instead, the lanthanides are a strong carrier suppressant, because their electronegativity (1.10–1.27, Supplementary Table 1) is much lower than Ga, and the Ln–O dissociation energy (397–799 kJ mol⁻¹, Supplementary Table 1) is much higher than Ga–O. To characterized the effect of Ln doping on the V_o concentration, XPS measurements of O 1s of undoped In₂O₃ and 14 Ln:In₂O₃ films were performed, as shown in Supplementary Fig. 3. The O 1s spectra can be fitted by three Gaussian distributions with binding energies at 529.5 ± 0.2 eV (Peak 1), 530.0 ± 0.2 eV (Peak 2), and 531.3 ± 0.3 eV (Peak 3), corresponding to the oxygen in oxide lattices (M–O–M), oxygen vacancies (V_o) and metal hydroxide (or loosely bound oxygen) species (M–OH), respectively³⁶. The $V_o/(M-O-M + V_o + M-OH)$ ratio for undoped In₂O₃ film is 18.3 %, while those for Ln:In₂O₃ (except Ce:In₂O₃) films are in the range of 10.8–4.1 %. The results prove that the Ln doping can effectively suppress V_o generation. It is worth noting that high-intensity M–OH peaks are observed in the XPS spectra of the La:In₂O₃ and Pr:In₂O₃ films, which may be attributed to larger radii of La³⁺ and Pr³⁺ compared to other trivalent Ln ions (except Ce which is mainly in the tetravalent state). Larger radius difference between In³⁺ and Ln³⁺ would cause more serious lattice mismatch and more loosely bound oxygen species. Interestingly, the Ce:In₂O₃ film has an extremely low V_o ratio of only 7.8% that is ascribed to the strong reducibility of Ce³⁺, which will further bind with oxygen atoms and oxidized to Ce⁴⁺ during annealing. Because the V_o concentration is very low in the Ce:In₂O₃ film, the free carrier density of it is very low, so almost

no field effects are found in the Ce:In₂O₃ TFTs. It should be noted that decreasing the Ce doping concentration will increase the I_{on} but will make the V_{on} more negative, as shown in Fig. S2. It is clear that doping Ce into In₂O₃ (in solution method) will deteriorate the performances of the Ce:In₂O₃ TFT (even with a small Ce doping amount of 0.8 at.%).

The mobilities of the TFTs based on 13 Ln:In₂O₃ (except Ce:In₂O₃) semiconductors are 3.1–6.1 cm² V⁻¹ s⁻¹ when annealed at 300 °C and 8.2–16.2 cm² V⁻¹ s⁻¹ when annealed at 350 °C (see Table 1 and Supplementary Fig. 4). The higher mobility with higher annealing temperature is attributed fewer impurities and a higher degree of order. Further increase the annealing temperature (>350 °C) has not tried, because the electrodes will be oxidized at higher annealing temperature. It can be seen from Table 1 that the mobility of the Eu:In₂O₃ and Yb:In₂O₃ TFTs are particularly low that may be due to the special electronic configurations of Eu (4f⁷6s²) and Yb (4f¹⁴6s²), which may lose two 6s electrons and form relatively stable Eu²⁺ (4f⁷) and Yb²⁺ (4f¹⁴). However, there are no direct evidences that Eu²⁺ and Yb²⁺ ions exist in the annealed solid films.

It is worth noting that the mobility of solution-processed AOS TFTs is generally lower than that of vacuum-based AOS TFTs because of the lower film quality and the impurities induced by the precursors. In our previous studies, the mobility of the vacuum-based Nd:In₂O₃ (5 at.%) TFT can reach as high as 46.4 cm² V⁻¹ s⁻¹, while the mobility of the solution-processed Nd:In₂O₃ (2 at.%) TFT is only 15.6 cm² V⁻¹ s⁻¹^{24,37}. The mobility of the TFTs with sputtered Pr/Tb:In₂O₃ (5 at.%) channel layer can reach as high as 36.2/38.1 cm² V⁻¹ s⁻¹ (not shown). The crystal structures of the solution-processed In₂O₃ and Tb:In₂O₃ films were investigated using X-ray diffraction (XRD), as shown in Supplementary Fig. 5. Both films exhibit clear nanocrystalline nature with In₂O₃ bixbyite structure, which is consistent with the standard value for bulk cubic-In₂O₃. Therefore, 5 at.% of Ln doping will not have a remarkable effect on the mobility of the In₂O₃.

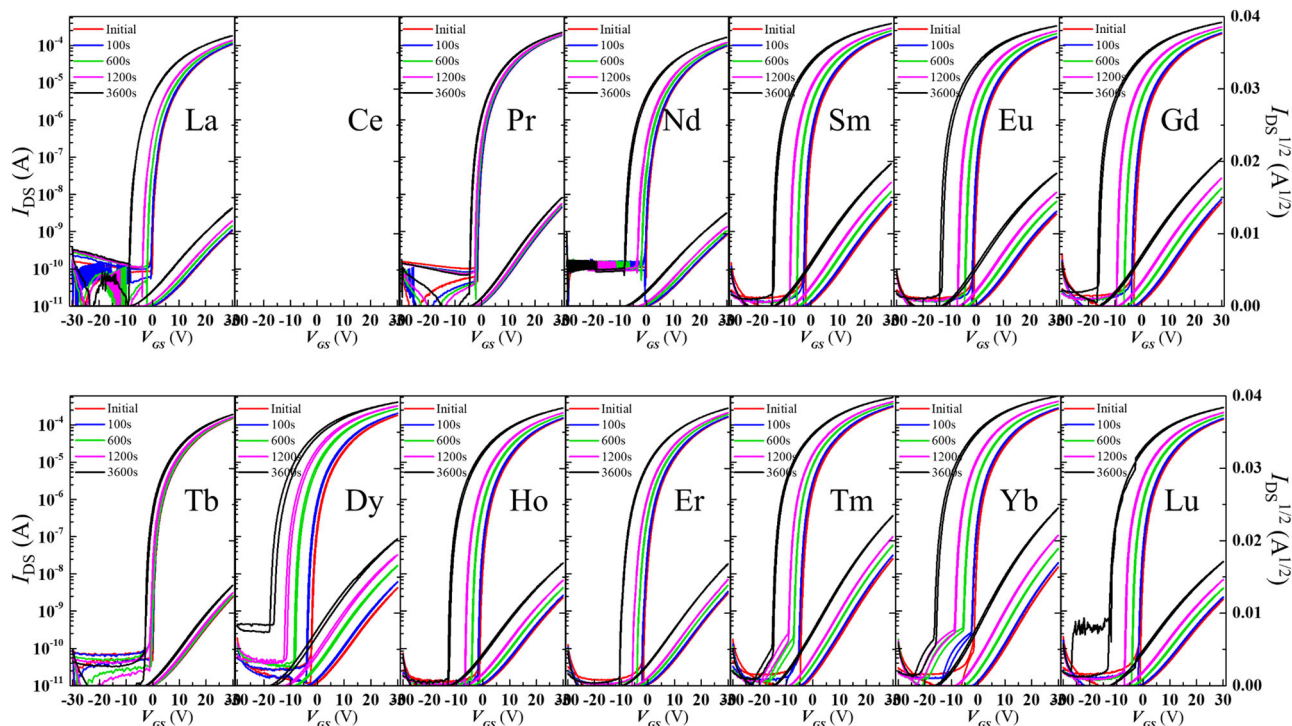


Fig. 5 NBIS stability of Ln:In₂O₃ TFTs. The variations of time-dependent transfer curves of the Ln: In₂O₃ TFTs when applied a negative gate bias stress of -20 V combining with white LED light illumination of 250 Lux.

The NBIS stability of the Ln:In₂O₃ TFTs. Supplementary Figure 6 shows the evolutions of transfer curves of the TFTs illuminated with different intensity of white light (without bias stress). The schematic diagram and the photo of the photostability testing equipment are shown in Supplementary Fig. 6. During illumination, the TFT channel was directly exposed to white LED light whose spectrum is depicted in Fig. 3b, and the intensity of the white light ranges from 500 to 5000 Lux. The undoped In₂O₃ TFT is rather unstable under the white light illumination, while the Pr:In₂O₃ and Tb:In₂O₃ TFTs are hardly affected by the white light illumination (highly stable even under 5000-Lux-light illumination, see Supplementary Fig. 7). For further investigating the effect of Ln doping on the photostability of the AOS TFTs, the devices were tested under the NBIS. During the NBIS, the TFTs were bias with a V_{GS} of -20 V under continuous white LED irradiation (250 Lux), and the transfer curves were recorded at 0, 100, 600, 1200, and 3600 s, respectively. Figure 5 shows the evolutions of the transfer curves of different TFTs as a function of the stress time. The V_{on} shift (ΔV_{on}) of the undoped In₂O₃ TFT is as large as -12.5 V (not shown), and the ΔV_{on} of the 13 Ln:In₂O₃ (except Ce:In₂O₃) TFTs are summarized in Table 1 and Supplementary Fig. 8. It is observed that the NBIS of the Pr:In₂O₃ and Tb:In₂O₃ TFTs are improved greatly, with the same ΔV_{on} of -3.0 V. The ΔV_{on} of the other 11 Ln:In₂O₃ TFTs are at the range of -7.9 to -15.6 V (see Table 1). The result shows that only the Pr and Tb are effective dopants for resolving the NBIS instability problem of the AOS TFTs.

It is known that high-density subgap states are formed by Vo existed in AOSs near valance band maximum (VBM). Under light illumination, some of the Vo will be thermal excited and lose two electrons and become Vo²⁺. The transition of the Vo ground state to Vo²⁺ excited states causes spontaneous outward relaxation, which makes the Vo²⁺ level act as a subgap state below the conduction band minimum (CBM), contributing the delocalized free electrons in the conduction band^{38–40}, as illustrated in Fig. 6. It has been reported that the formation

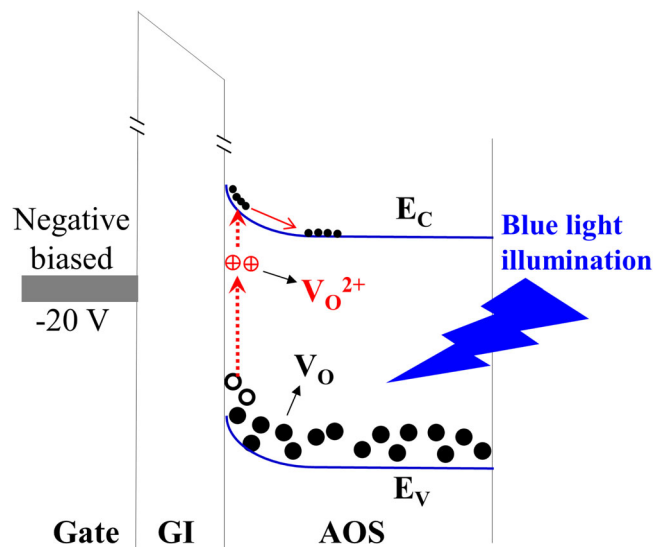


Fig. 6 The origin of NBIS in stability for AOS TFTs. The schematic diagram for generation of Vo²⁺ in AOS TFTs under NBIS.

energy of Vo²⁺ decreases as the fermi lever (E_F) approaching the VBM³⁸. When a negative bias is applied to the gate electrode, the energy band at the gate insulator (GI)/AOS interface bends up, so the E_F is closer to the VBM (see Fig. 6). As a result, the formation energy of Vo²⁺ at the GI/AOS interface decreases. Therefore, more Vo²⁺ will be formed when a negative V_{GS} is applied during light illumination (NBIS), leading to more electrons in the conduction band, which is the reason for the large negative V_{on} shift under the NBIS. Meanwhile, the ΔV_{on} is increase with illumination intensity (as seen in Supplementary Fig. 9). The photoresponse is reversible very slowly with a time constant exceeding thousands of seconds. This is attributed to the

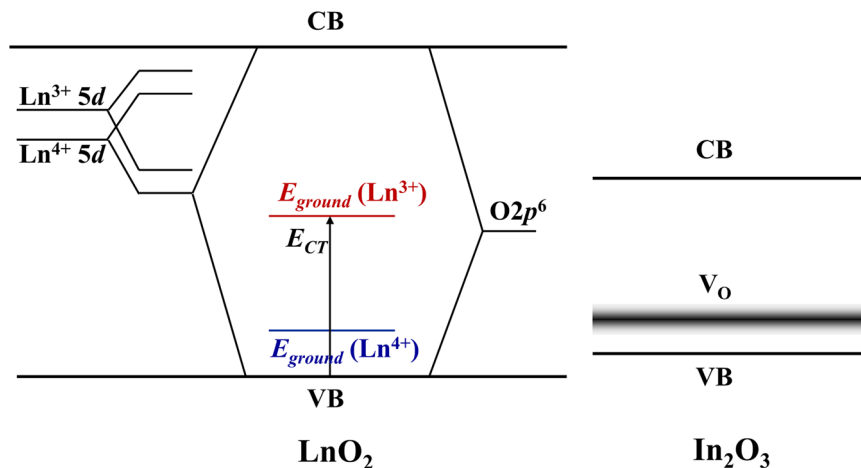


Fig. 7 The schematic diagram of energy levels of the tetravalent lanthanide oxides and In_2O_3 . The valence band (VB) and the conduction band (CB) were formed by bonding orbitals and antibonding orbitals consisted of the $\text{Ln}5d$ orbitals and the $\text{O}2p$ orbitals in lanthanide oxides.

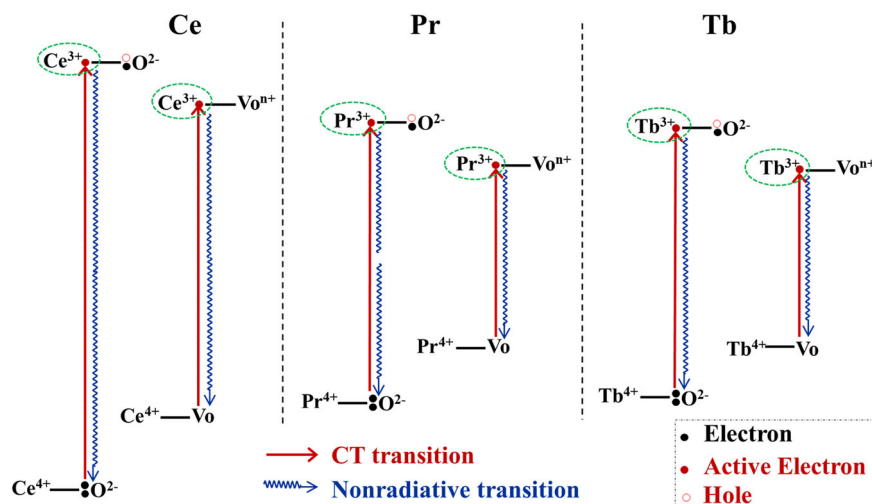


Fig. 8 The schematic diagram of charge transfer transition for Ce^{4+} , Tb^{4+} , and Pr^{4+} . The hole in $\text{O}2p^{-1}$ will pull the transitioned electron back to its original space by a nonradiative way.

relaxation of metastable donor states with activation energies of 0.9–1.1 eV^{3,4}.

The effect of Pr and Tb in NBIS stability. It can be deduced from the analysis above that there are mainly three ways to improve the NBIS stability of the AOS TFTs. i) to decrease the Vo concentration; ii) to widen the bandgap of the AOSs and deepen the VBM and the Vo subgap states, so that the Vo cannot be activated by the visible light; iii) to downconvert the incident light by doping some lanthanide ions into the AOSs, so that the energy of the output light is not enough to activate the Vo. Here, the excellent NBIS stability of the $\text{Pr}:\text{In}_2\text{O}_3$ and $\text{Tb}:\text{In}_2\text{O}_3$ TFTs cannot be attributed to the suppression of Vo, because there is no evident relationship between the Vo ratios and the ΔV_{on} under the NBIS (see Table 1 and Supplementary Table 1). The VBMs of the $\text{Ln}:\text{In}_2\text{O}_3$ thin films were characterized by ultraviolet photoelectron spectroscopy (UPS) measurements. It is found that there is no much difference on the VBMs for all of the 14 $\text{Ln}:\text{In}_2\text{O}_3$ films (Supplementary Fig. 10), so the much better NBIS stability of the $\text{Pr}:\text{In}_2\text{O}_3$ and $\text{Tb}:\text{In}_2\text{O}_3$ TFTs compared to the other $\text{Ln}:\text{In}_2\text{O}_3$ TFTs cannot be attributed to the bandgap widening. Therefore, the excellent NBIS stability of the $\text{Pr}:\text{In}_2\text{O}_3$ and $\text{Tb}:\text{In}_2\text{O}_3$ TFTs is probably due to the downconversion effect of the Pr and Tb ions.

As discussed at the beginning of this section, the CeO_x , PrO_x , and TbO_x films exhibit broad-band absorption (see Fig. 2), while the other films are transparent to the light with the wavelength longer than 300 nm; and the broad-band and strong absorption the CeO_x , PrO_x , and TbO_x films are mainly resulted from the charge transfer transition from ligands to $\text{Ln} 4f$. Among all of the lanthanides, only Ce, Pr, Tb, Nd, and Dy have tetravalent oxidation states, but Nd^{4+} and Dy^{4+} are very unstable because of their large III–IV potentials (E^0 , see Supplementary Table 1)⁴¹. The stability sequence of the tetravalent oxidation states is $\text{Ce}^{4+} > \text{Tb}^{4+} \approx \text{Pr}^{4+} \gg \text{Nd}^{4+} > \text{Dy}^{4+}$. In lanthanide oxides, the $\text{Ln}5d$ orbitals and the $\text{O}2p$ orbitals make up the chemical bonds; the bonding orbitals form the valence band (VB), and antibonding orbitals form the conduction band (CB), as illustrated in Fig. 7. So, the charge transfer energy (E_{CT}) is the difference between the ground state of the Ln^{3+} (E_{ground}) and the energy level of VBM (E_{V}):

$$E_{\text{CT}} = E_{\text{ground}}(\text{Ln}^{3+}) - E_{\text{V}} \quad (1)$$

The E_{CT} of Ce (III–IV) can be calculated from the charge transfer absorption peak (300 nm, see Fig. 2c) to be 4.1 eV. The E_{CT} of Pr (III–IV) and Tb (III–IV) should be estimated from the E_{CT} of Ce (III–IV), because the PrO_x and TbO_x do not display a

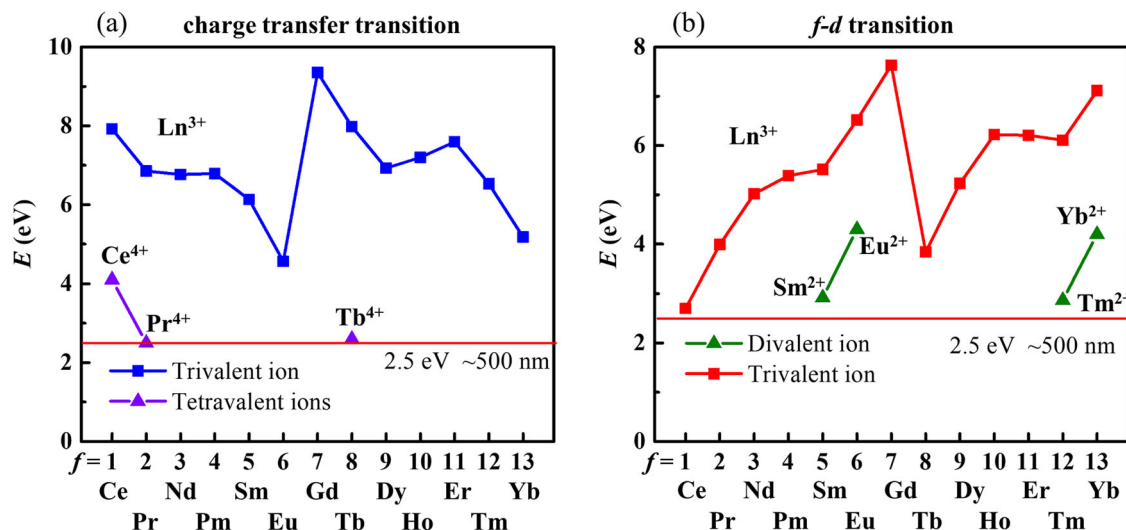


Fig. 9 The energy of transition. **a, b** The energy required for (a) charge transfer and (b) f - d transition of Ln^{3+} and Ln^{4+} ions.

well-resolved charge transfer absorption band (Figs. 2d, e). L.J. Nugent et al.⁴¹ reported that there is a linear unit-slope relationship between the III–IV potentials (E^0) and the first charge transfer band energy. Although they did not provide the formulas for the relationship between the E_{CT} and E^0 , it can be deduced from plots of the E^0 versus the first absorption energy that E_{CT} of Pr/Tb can be expressed as

$$E_{\text{CT}}(\text{Ln}) = E_{\text{CT}}(\text{Ce}) + C[E^0(\text{Ce}) - E^0(\text{Ln})] \quad (2)$$

where C is a constant estimated to be -1 eV V^{-1} . It can be calculated from Eq. 2 that E_{CT} of Pr and Tb (III–IV) are 2.5 eV (496 nm) and 2.6 eV (477 nm), respectively. Therefore, the charge transfer absorption peaks of PrO_x and TbO_x enter the blue light regime even without considering the electron cloud expansion effect.

Because Ce^{4+} is most stable, the energy level of Ce^{4+} is lowest. It means that, higher energy is required for charge transfer transition from $|\text{Ce}4f^0\rangle$ to $|\text{Ce}4f^1\text{O}2p^{-1}\rangle$, compared to those from $|\text{Pr}4f^1\rangle$ to $|\text{Pr}4f^2\text{O}2p^{-1}\rangle$ or from $|\text{Tb}4f^7\rangle$ to $|\text{Tb}4f^8\text{O}2p^{-1}\rangle$, as illustrated in Fig. 8. After charge transfer transition, the hole in $\text{O}2p^{-1}$ will pull the transitioned electron back to its original space by a nonradiative way (or downconverted to red light). Supplementary Fig. 11 shows the enhanced photoluminescence spectra of the $\text{Ce}:\text{In}_2\text{O}_3$, $\text{Pr}:\text{In}_2\text{O}_3$, and $\text{Tb}:\text{In}_2\text{O}_3$ films stimulated by high-intensity 450-nm light. Only $\text{Pr}:\text{In}_2\text{O}_3$ shows a weak red-light peak centered at ~ 625 nm. So it can be deduced that the absorbed incident light is converted to lattice vibration for the $\text{Ce}:\text{In}_2\text{O}_3$ and $\text{Tb}:\text{In}_2\text{O}_3$ films, and a small part of the absorbed incident light is converted to red light for the $\text{Pr}:\text{In}_2\text{O}_3$ film. It should be noted that the Ln^{4+} ions tend to move to V_o , because of the weak electrostatic attraction, and the charge transfer transition is more easily to take place between V_o and Ln^{4+} , so it can absorb light with lower energy (longer wavelength), as illustrated in Fig. 8. T. Kamiya et al.² reported that amorphous IGZO TFTs respond to photon energies above 2.3 eV (corresponding to the wave lengths below 540 nm), which is lower than the bandgap (3.1 eV). It means that the blue light and parts of the green light of the LED light are responsible for the photoinstability of the AOS TFTs. It can be observed from Figs. 2d, e that the absorption spectra for both of the PrO_x and TbO_x films extend to the near-infrared region, so they can absorb almost the whole range of the incident white LED light (see Fig. 3b). As a result, the incident white LED light is downconverted to the

nonradiative transition by Pr^{4+} or Tb^{4+} that enhances the NBIS stability greatly.

It should be noted that the charge transfer transition energies of the $\text{Ln}^{3+} \rightarrow \text{Ln}^{2+}$ is much higher than those of $\text{Ln}^{4+} \rightarrow \text{Ln}^{3+}$, as shown in Fig. 9a, so the $\text{Ln}^{3+} \rightarrow \text{Ln}^{2+}$ transition cannot absorb blue light. As a result, the Ln^{3+} ions cannot improve the photostability of the TFTs.

Besides tetravalent ions, trivalent ions also exist in the CeO_x , PrO_x , and TbO_x films. That means $4f$ - $5d$ transition is likely to take place, because the f - d transition energies (E_{fd}) for Ce^{3+} , Pr^{3+} , and Tb^{3+} ions are much lower than those for other free Ln^{3+} ions (see Supplementary Table 1). It is known that the E_{fd} can be lower greatly by choosing ligands with lower electronegativity due to the larger metal-ligand electron cloud overlap (electron cloud expansion effect). Different from the f - f transition, the f - d transition is allowed by the parity selection rule, so it has a fairly high transition intensity that is 10^6 times higher than f - f transition. And f - d transition has a wide absorption band because the $5d$ energy level is widened by ligand ions. Since the E_{fd} for Ce^{3+} is lower than that for Pr^{3+} or Tb^{3+} , and the light absorption spectrum of the CeO_x film is cut-off at ~ 390 nm (Fig. 1e), it can be deduced that the light energy for the f - d transition for all of the CeO_x , PrO_x , and TbO_x films should be greater than 3.18 eV (< 390 nm). It means that the visible light absorption of the PrO_x and TbO_x films cannot be attributed to the f - d transition. Therefore, the charge transfer transition is the only reason for the greatly improved NBIS stability of the TFTs with the $\text{Pr}:\text{In}_2\text{O}_3$ or $\text{Tb}:\text{In}_2\text{O}_3$ semiconductor layers.

It is worth noting that the bivalent Ln ions (Ln^{2+}) have lower E_{fd} than the trivalent Ln ions (Ln^{3+}). And the E_{fd} of some Ln^{2+} ions are close to the energy of blue light. For example, the E_{fd} for Eu^{2+} , Yb^{2+} , Sm^{2+} , and Tm^{2+} are 4.30, 4.20, 2.92, and 2.87 eV, respectively (see Fig. 9b). However, only Eu^{2+} and Yb^{2+} are stable in the solid state. Moreover, the $\text{Ln}:\text{In}_2\text{O}_3$ films must experience high-temperature annealing ($> 300^\circ\text{C}$), so the Ln^{2+} ions will be oxidized to Ln^{3+} ions. Thus, it is difficult to achieve stable AOS TFTs doped with Ln^{2+} ions.

It is worth noting that the $\text{Pr}:\text{In}_2\text{O}_3$ and $\text{Tb}:\text{In}_2\text{O}_3$ TFTs exhibit worsened stability under positive bias illumination stress (PBIS) with ΔV_{on} of 1.1 and 0.9 V, respectively (see Supplementary Fig. 12). The degradation of the PBIS for $\text{Pr}:\text{In}_2\text{O}_3$ and $\text{Tb}:\text{In}_2\text{O}_3$ TFTs is ascribed to the light-induced shallow electron traps (possibly Pr^{3+} and Tb^{3+} related defects).

Supplementary Figures 13 and 14 show the stability under negative bias temperature stress (NBTS) and positive bias temperature stress (PBTS) of different TFTs at 60 °C without light illumination, respectively. The ΔV_{on} for all the TFTs under NBTS, PBTS, and PBIS are summarized in Supplementary Table 2. The pure In_2O_3 TFT exhibits poor NBTS stability, while all of the Ln: In_2O_3 TFTs have good NBTS stability. In contrary to the NBTS stability, the PBTS stability of the pure In_2O_3 TFT is good (see Supplementary Fig. 14), which may be attributed to the much higher free electron density than the electron traps in the In_2O_3 film. However, most Ln: In_2O_3 TFTs show relatively poor PBTS (especially the La, Nd, and Ho incorporated In_2O_3 TFTs). It reveals that incorporating Ln to In_2O_3 will induce shallow electron traps in the In_2O_3 films. The temperature effect of the Ln: In_2O_3 TFTs is still under investigated, and will be published in the future.

Conclusions

In conclusion, the effect of different lanthanide dopants on the NBIS stability of solution-processed AOS TFTs are investigated. Compared to the undoped In_2O_3 TFT, which has a turn-on voltage (V_{on}) of -13.3 V, the lanthanide-doped In_2O_3 (Ln: In_2O_3) TFTs have more positive V_{on} that range from -1 to 1 V and more steeper SS, revealing that Ln doping with a concentration of only 5 at.% can suppress oxygen vacancy (Vo) generation and decrease free carrier concentration substantially. More interestingly, the NBIS stability of the TFTs are improved greatly when the In_2O_3 AOS is doped by praseodymium (Pr) or terbium (Tb). The Pr: In_2O_3 and Tb: In_2O_3 TFTs exhibit the same V_{on} shift (ΔV_{on}) of -3.0 V, compared to a ΔV_{on} of as high as -12.0 V of the undoped In_2O_3 TFT. The NBIS stability of the In_2O_3 TFTs doped with the other lanthanides are not good, with ΔV_{on} at the range of -7.9 to -15.6 V. The mobility of the solution-processed Pr: In_2O_3 and Tb: In_2O_3 TFTs are 12.2 and 12.7 cm^2 V^{-1} s^{-1} , respectively. Comprehensive studies reveal that Pr/Tb acts as not only a Vo suppressant but also a blue light downconversion medium with low charge transfer transition energy. Most of the incident white light can be absorbed by Pr^{4+} or Tb^{4+} ions by charge transfer transition, and downconverted to nonradiative transition or red light. As a result, the NBIS stability of the AOS TFTs is improved greatly. The result is different from those reported elsewhere, where the lanthanides are merely regarded as free carrier suppressants of the AOSs due to ultra-low electronegativities

Methods

Materials. The metal oxide semiconductor films were deposited by spin-coating and thermal decomposition of precursors solution. A 0.2 M In_2O_3 solution was prepared by dissolving indium nitrate hydrate ($(\text{In}(\text{NO}_3)_3 \cdot n\text{H}_2\text{O})$, Sigma-Aldrich) in deionized water. The Ln: In_2O_3 precursors solutions were synthesized by dissolving indium nitrate hydrate ($(\text{In}(\text{NO}_3)_3 \cdot n\text{H}_2\text{O})$, Sigma-Aldrich) and lanthanides nitrate hydrate ($(\text{La}(\text{NO}_3)_3 \cdot n\text{H}_2\text{O})$, $(\text{Ce}(\text{NO}_3)_3 \cdot n\text{H}_2\text{O})$, $(\text{Pr}(\text{NO}_3)_3 \cdot n\text{H}_2\text{O})$, $(\text{Nd}(\text{NO}_3)_3 \cdot n\text{H}_2\text{O})$, $(\text{Sm}(\text{NO}_3)_3 \cdot n\text{H}_2\text{O})$, $(\text{Eu}(\text{NO}_3)_3 \cdot n\text{H}_2\text{O})$, $(\text{Gd}(\text{NO}_3)_3 \cdot n\text{H}_2\text{O})$, $(\text{Tb}(\text{NO}_3)_3 \cdot n\text{H}_2\text{O})$, $(\text{Dy}(\text{NO}_3)_3 \cdot n\text{H}_2\text{O})$, $(\text{Ho}(\text{NO}_3)_3 \cdot n\text{H}_2\text{O})$, $(\text{Er}(\text{NO}_3)_3 \cdot n\text{H}_2\text{O})$, $(\text{Tm}(\text{NO}_3)_3 \cdot n\text{H}_2\text{O})$, $(\text{Yb}(\text{NO}_3)_3 \cdot n\text{H}_2\text{O})$, $(\text{Lu}(\text{NO}_3)_3 \cdot n\text{H}_2\text{O})$, aladdin) in deionized water, which was optimized to the total concentration of metal ion of 0.2 M and Ln/In molar ratio of 19:1. All the precursor solutions were stirred vigorously for 12 h at room temperature and filtered through a 0.22 μm syringe filter before spin-coating.

Devices fabrication. A bottom-gate and top-contact source-drain electrode structure was used to fabricate Ln: In_2O_3 TFT. Firstly a 200 -nm thickness Al_2O_3 :Nd gate dielectric layer with a capacitance density of 38 nF cm^{-2} was formed by anodization on the surface of a 300 -nm thick Al:Nd alloy film deposited on glass by sputtering and patterned by wet etch, which the details process have been reported in our previous report. Then, the substrates were cleaned ultrasonically in deionized water and isopropanol for 10 min, respectively, and dried in an air oven of 80 °C. Next, an ultraviolet light irradiating of a long time was used to treat a part (channel area) of the Al_2O_3 :Nd surface with a stencil shadow mask, for the formation of a hydrophilic surface in the channel area. The Ln: In_2O_3 precursor films were deposited in the wettable area irradiated by UV by spin-coating Ln: In_2O_3

precursor solutions at 2000 rpm for 5 s and 6500 rpm for 40 s, followed by drying at 40 °C and thermal annealing at $300/350$ °C for 1 h in an air condition. Finally, the Al source and drain electrodes were deposited on the Ln: In_2O_3 layer by thermal evaporation, defined the channel area with 1000 μm width and 300 μm length by using a stencil shadow mask.

Devices characterization. The electrical characteristics of undoped In_2O_3 and Ln: In_2O_3 TFTs were measured using a semiconductor parameter analyzer system (Agilent B1500A) in conjunction with a probe station (Lakeshore CRX-VF) at room temperature and air condition. The NBIS stability was tested by monitoring evolutions of the transfer curves of MO TFTs based on a series of Ln incorporated In_2O_3 semiconductors as a function of the stress time under gate bias stresses of -20 V combining with white LED irradiation of optical density of 250 Lux, respectively. The energy levels of the functional layer were measured with Ultra-violet Photoelectron Spectrometer (UPS) of K-ALPHA⁺ of Thermo Fisher Scientific. The absorption spectrum was measured by using UV-2600. The enhanced photoluminescence spectra was measured by using FLS1000. The X-ray Photoelectron Spectroscopy (XPS) was measured by using K-ALPHA⁺ of Thermo Fisher Scientific with Mono AlKa. The carrier mobility for the saturation regime was calculated using:

$$I_{Ds} = \frac{W\mu C_i}{2L}(V_{GS} - V_{th})^2 \quad (3)$$

where μ is the field-effect mobility, C_i is the areal capacitance per area of the gate dielectric, V_{th} is the threshold voltage, W is the channel width, and L is the channel length.

Data availability

The data that support the plots within this paper and other findings of this study are available from the corresponding authors upon reasonable request.

Received: 4 January 2021; Accepted: 29 July 2021;

Published online: 23 August 2021

References

- Nomura, K. et al. Room-temperature fabrication of transparent flexible thin-film transistors using amorphous oxide semiconductors. *Nature*. **432**, 488–492 (2004).
- Kamiya, T., Nomura, K. & Hosono, H. Present status of amorphous In-Ga-Zn-O thin-film transistors. *Sci Technol Adv. Mater.* **11**, 44305 (2010).
- Takechi, K., Nakata, M., Eguchi, T., Yamaguchi, H. & Kaneko, S. Comparison of ultraviolet photo-field effects between hydrogenated amorphous silicon and amorphous InGaZnO₄ thin-film transistors. *Jpn. J. Appl. Phys.* **48**, 010203 (2009).
- Lee, D. H., Kawamura, K., Nomura, K., Kamiya, T. & Hosono, H. Large photoresponse in amorphous In-Ga-Zn-O and origin of reversible and slow decay. *Electrochem. Solid-State Lett.* **13**, H324–H327 (2010).
- Jeong, J. K. Photo-bias instability of metal oxide thin film transistors for advanced active matrix displays. *J. Mater. Res.* **28**, 2071–2084 (2013).
- Shin, J. et al. Light effects on the bias stability of transparent ZnO thin film transistors. *Etri J.* **31**, 62–64 (2009).
- Lee, K. et al. The effect of moisture on the photon-enhanced negative bias thermal instability in Ga-In-Zn-O thin film transistors. *Appl. Phys. Lett.* **95**, 232106 (2009).
- Son, K. et al. Improvement of photo-induced negative bias stability of oxide thin film transistors by reducing the density of sub-gap states related to oxygen vacancies. *Appl. Phys. Lett.* **102**, 122108 (2013).
- Ji, K. H. et al. Comparative study on light-induced bias stress instability of IGZO transistors with SiN_x and SiO₂ gate dielectrics. *IEEE Electron Device Lett.* **31**, 1404–1406 (2010).
- Chowdhury, M. D. H., Migliorato, P. & Jang, J. Light induced instabilities in amorphous indium-gallium-zinc-oxide thin-film transistors. *Appl. Phys. Lett.* **97**, 173506 (2010).
- Oh, H. et al. Photon-accelerated negative bias instability involving subgap states creation in amorphous In-Ga-Zn-O thin film transistor. *Appl. Phys. Lett.* **97**, 183502 (2010).
- Nahm, H., Kim, Y. & Kim, D. H. Instability of amorphous oxide semiconductors via carrier-mediated structural transition between disorder and peroxide state. *Phys. Status Solidi B.* **249**, 1277–1281 (2012).
- De Jamblinne De Meux, A., Pourtois, G., Genoe, J. & Heremans, P. Effects of hole self-trapping by polarons on transport and negative bias illumination stress in amorphous-IGZO. *J. Appl. Phys.* **123**, 161513 (2018).
- Yang, B. S. et al. Role of ZrO₂ incorporation in the suppression of negative bias illumination-induced instability in Zn-Sn-O thin film transistors. *Appl. Phys. Lett.* **98**, 122110 (2011).

15. Lan, L. et al. Improving negative-bias-temperature-stress stability for thin-film transistors by doping Mg into ScInO semiconductor. *IEEE Trans. Electron Devices*. **66**, 2620–2623 (2019).
16. Long, T. et al. High-performance CdScInO thin-film transistors and their stability improvement under negative bias (illumination) temperature stress. *J. Mater. Chem. C*. **7**, 13960–13965 (2019).
17. Ji, K. H. et al. Effect of high-pressure oxygen annealing on negative bias illumination stress-induced instability of InGaZnO thin film transistors. *Appl. Phys. Lett.* **98**, 103509 (2011).
18. Yeob Park, S. et al. Improvement in the device performance of tin-doped indium oxide transistor by oxygen high pressure annealing at 150 °C. *Appl. Phys. Lett.* **100**, 162108 (2012).
19. Son, K. et al. Improvement of photo-induced negative bias stability of oxide thin film transistors by reducing the density of sub-gap states related to oxygen vacancies. *Appl. Phys. Lett.* **102**, 122108 (2013).
20. Yang, S. et al. Suppression in the negative bias illumination instability of Zn-Sn-O transistor using oxygen plasma treatment. *Appl. Phys. Lett.* **99**, 102103 (2011).
21. Yang, B. S. et al. Improvement of the photo-bias stability of the Zn-Sn-O field effect transistors by an ozone treatment. *J. Mater. Chem.* **22**, 10994 (2012).
22. Kim, J., Bang, J., Nakamura, N. & Hosono, H. Ultra-wide bandgap amorphous oxide semiconductors for NBIS-free thin-film transistors. *APL Mater.* **7**, 22501 (2019).
23. Jang, J. T., Choi, S., Kim, D. M. & Kim, D. H. The calculation of negative bias illumination stress-induced instability of amorphous InGaZnO thin-film transistors for instability-aware design. *IEEE Trans. Electron Devices*. **65**, 1002–1008 (2018).
24. Lin, Z. et al. Studies on Nd_xIn_{1-x}O₃ semiconducting thin films prepared by rf magnetron sputtering. *Appl. Phys. Lett.* **105**, 142104 (2014).
25. Lin, Z. et al. Effects of rare-earth element dopants in high-mobility InO_x-based thin-film transistors. *IEEE Electr. Device Lett.* **37**, 1139–1142 (2016).
26. Li, M. et al. Improving thermal stability of solution-processed indium zinc oxide thin-film transistors by praseodymium oxide doping. *ACS Appl. Mater. Interfaces*. **10**, 28764–28771 (2018).
27. Xu, H. et al. Trap-assisted enhanced bias illumination stability of oxide thin film transistor by praseodymium doping. *ACS Appl. Mater. Interfaces*. **11**, 5232–5239 (2019).
28. Ren, J. et al. Effects of rare-earth erbium doping on the electrical performance of tin-oxide thin film transistors. *J. Alloys Compd.* **791**, 11–18 (2019).
29. Ren, J. et al. Preparation of rare-earth thulium doped tin-oxide thin films and their applications in thin film transistors. *Appl. Surf. Sci.* **493**, 63–69 (2019).
30. Yang, J., Hu, G., Cao, D. & Liu, F. Communication-wide bandgap tin oxide thin film transistor by doping rare earth element europium. *ECS J. Solid State Sci. Technol.* **9**, 65004 (2020).
31. Kim, J. et al. Room-temperature fabrication of light-emitting thin films based on amorphous oxide semiconductor. *AIP Adv.* **6**, 15106 (2016).
32. Watanabe, N. et al. Multiple color inorganic thin-film phosphor, RE-doped amorphous gallium oxide (RE = rare earth: Pr, Sm, Tb, and Dy), deposited at room temperature. *Phys. Status Solidi A*. **216**, 1700833 (2018).
33. Hobart, D. E. et al. Stabilization of praseodymium (IV) and terbium (IV) in aqueous carbonate solution. *Inorg. Nucl. Chem. Lett.* **16**, 321–328 (1980).
34. Gao, P. et al. Low-temperature, high-mobility, solution-processed metal oxide semiconductors fabricated with oxygen radical assisted perchlorate aqueous precursors. *Chem. Commun.* **53**, 6436–6439 (2017).
35. Song, W. et al. Low-temperature, high-stability, flexible thin-film transistors with a novel Sc_xIn_{1-x}O₃ semiconductor. *J. Phys. D Appl. Phys.* **49**, 24LT01 (2016).
36. Cho, S. W. et al. Chemical durability engineering of solution-processed oxide thin films and its application in chemically-robust patterned oxide thin-film transistors. *J. Mater. Chem. C*. **5**, 339–349 (2017).
37. Lin, Z. et al. Solution-processed high-mobility neodymium-substituted indium oxide thin-film transistors formed by facile patterning based on aqueous precursors. *Appl. Phys. Lett.* **110**, 133502 (2017).
38. Janotti, A. & Van de Walle, C. G. Oxygen vacancies in ZnO. *Appl. Phys. Lett.* **87**, 122102 (2005).
39. Lany, S. & Zunger, A. Anion vacancies as a source of persistent photoconductivity in II-VI and chalcopyrite semiconductors. *Phys. Rev. B*. **72**, 035215 (2005).
40. Janotti, A. & Van de Walle, C. G. Native point defects in ZnO. *Phys. Rev. B*. **76**, 165202 (2007).
41. Nugent, L. J., Baybarz, R. D., Burnett, J. L. & Ryan, J. L. Electron-transfer and f→d absorption bands of some lanthanide and actinide complexes and the standard (III-IV) oxidation potentials for each member of the lanthanide and actinide series. *J. Inorg. Nucl. Chem.* **33**, 2503–2530 (1971).

Acknowledgements

This work was supported by the National Natural Science Foundation of China (Grant Nos. 62022034, 51673068, 62074059), the Guangdong Natural Science Foundation (Grant No. 2017A030306007), the Guangdong Project of R&D Plan in Key Areas (Grant Nos. 2020B010180001, and 2019B010934001), and the Guangdong Major Project of Basic and Applied Basic Research (No. 2019B030302007).

Author contributions

L.F.L., P.H.H., and J.B.P. presented the idea and designed the experiment. P.H.H., C.C.D., and X.L. fabricated the devices. Y.B.W. and S.T.C. performed XPS measurements. Y.L.L. performed XRD measurements. P.H.H., C.H.D. carried out NBIS and PBIS measurements. M.X. and H.X. carried out NBTS and PBTS measurements. P.H.H. and L.F.L. wrote this manuscript. All authors participated in interpretation of the results and manuscript preparation.

Competing interests

The authors declare no competing interests.

Additional information

Supplementary information The online version contains supplementary material available at <https://doi.org/10.1038/s43246-021-00193-4>.

Correspondence and requests for materials should be addressed to L.L.

Peer review information *Communications Materials* thanks Junghwan Kim and the other, anonymous, reviewer(s) for their contribution to the peer review of this work. Primary Handling Editors: Aldo Isidori.

Reprints and permission information is available at <http://www.nature.com/reprints>

Publisher's note Springer Nature remains neutral with regard to jurisdictional claims in published maps and institutional affiliations.



Open Access This article is licensed under a Creative Commons Attribution 4.0 International License, which permits use, sharing, adaptation, distribution and reproduction in any medium or format, as long as you give appropriate credit to the original author(s) and the source, provide a link to the Creative Commons license, and indicate if changes were made. The images or other third party material in this article are included in the article's Creative Commons license, unless indicated otherwise in a credit line to the material. If material is not included in the article's Creative Commons license and your intended use is not permitted by statutory regulation or exceeds the permitted use, you will need to obtain permission directly from the copyright holder. To view a copy of this license, visit <http://creativecommons.org/licenses/by/4.0/>.

© The Author(s) 2021